Available online at https://link.springer.com/journal/42241
http://www.jhydrodynamics.com
Journal of Hydrodynamics, 2023, 35(4): 649-667
https://doi.org/10.1007/s42241-023-0051-x

Numerical investigations on performance improvement mechanism of a high-power vertical centrifugal pump with special emphasis on hydraulic component matching

Gang Yang[1], Xi Shen[1, 2], De-sheng Zhang[1*], Wen-hua Luo[1], Jia Meng[1], Xu-tao Zhao[1]
1. *Research Center of Fluid Machinery Engineering and Technology, Jiangsu University, Zhenjiang 212013, China*
2. *Key Laboratory of Fluid Machinery and Engineering, Xihua University, Chengdu 610039, China*

(Received March 16, 2023, Revised April 20, 2023, Accepted May 12, 2023, Published online September 21, 2023)

Abstract: The purpose of this paper is to investigate the performance improvement mechanism of a high power vertical centrifugal pump by using numerical calculations. Therefore, a comparative study of energy losses and internal flow characteristics in the original and optimized models was carried out with special attention to the hydraulic component matching. The optimized model (model B) was obtained by optimizing the vaned diffuser and volute based on the original model (model A), mainly the diffuser inlet diameter, diffuser inlet vane angle, volute channel inlet width and volute throat area were changed. Firstly, the comparative results on performance and energy losses of two models showed that the efficiency and head of model B was significantly increased under design and part-load conditions. It is mainly due to the dramatic reduction of energy loss P_L in the diffuser and volute. Then, the comparisons of P_L and flow patterns in the vaned diffuser showed that the matching optimization between the model B impeller outlet flow angle and diffuser inlet vane angle resulted in a better flow pattern in both the circumferential and axial directions of the diffuser, which leads to the P_{L3} reduction. The meridian velocity V_m of model B was significantly increased at diffuser inlet regions and resulted in improvements of flow patterns at diffuser middle and outlet regions as well as pressure expansion capacity. Finally, the comparisons of P_L and flow characteristics in the volute showed that the turbulence loss reduction in the model B volute was due to the flow pattern improvement at diffuser outlet regions which provided better flow conditions at volute inlet regions. The matching optimization between the diffuser and volute significantly reduced the turbulence loss in volute sections 1-4 and enhanced the pressure expansion capacity in sections 8-10.

Key words: High-power vertical centrifugal pump, performance improvement mechanism, hydraulic component matching, flow pattern, energy balance equation

0. Introduction

The energy resources on earth are abundant and hydro energy is considered a promising huge energy. As one of the core equipment for exploiting and utilizing hydro energy, high-power vertical centrifugal pumps (HVCP) are widely used in pumped storage power system, cross-basin water transfer and other projects[1-3]. HVCP are characterized by its widely applications, high power (usually reach megawatt level) and long operation time, resulting in its energy consumptions account for significant proportion of global energy consumption. Under the guidance of peak carbon dioxide emissions and carbon neutrality, it is urgent to effectively improve the performance of HVCP. The vaned diffuser plays a critical role in HVCP, but it also makes the design of high matching between hydraulic components more difficult. Meanwhile, the hydraulic component matching is the key factor to determine the performance of HVCP[4-5]. Hence, it would be meaningful to study the hydraulic component matching and performance variation mechanism based on numerical simulations for efficient and energy-saving design of HVCP.

In conventional centrifugal pumps with vaneless diffuser structure, many scholars analyzed the hydraulic performance and flow patterns in detail by combining simulations and experiments[6-7]. Research hotspots include hump characteristics under part-load

Project supported by the National Natural Science Foundation of China (Grant No. 51979125).
Biography: Gang Yang (1997-), Male, Ph. D. Candidate,
E-mail: harbor_yang2022@outlook.com
Corresponding author: De-sheng Zhang,
E-mail: zds@ujs.edu.cn

conditions[8-9], rotor-stator interactions between impeller and volute tongue[10-11], as well as cavitation etc.[12-13]. For HVCP, they usually have a stay vaned diffuser structure to meet the hydraulic design requirements[14-15]. The vaned diffuser is installed between the impeller and volute, which increases the complexity of hydraulic structures. Hence, the matching problem of the hydraulic components is more prominent in HVCP. Li et al.[16] studied the matching characteristics of the impellers and guide vanes of a high-pressure seawater desalination pump in terms of the impeller blade outlet width, the number of impeller and guide vane blades, and the area ratio of impeller outlet to guide vane inlet. The results showed that properly increase the number of guide vane blades or change the number of impeller blades can improve efficiency and expand the high-efficiency region. Zeng et al.[17] investigated the effect on lean mode of the blade trailing edge on the hydraulic performance and pressure fluctuation of a vertical centrifugal pump with vaned diffuser. The results showed that the lean mode of blade trailing edge had little influence on the hydraulic performance. The flow peak-to-peak value of average pressure fluctuation in the positive lean mode was 62% of the corresponding value in zero lean mode. Lu[18] investigated the effect of matching relationship between impeller and vaned diffuser on the performance and flow pattern of stamping centrifugal pump. The main results showed that an increase in the ratio between impeller outlet and vaned diffuser inlet areas and a reduction in the axial distance between impeller and vaned diffuser could both effectively improve the pump performance. Zhu et al.[19] investigated the effect of impeller blade lean on the flow pattern and performance of a pump-turbine. Two impellers with large positive and negative blade lean were designed for numerical and experimental analysis. The results showed that the negative blade lean could control the flow separation on the high-pressure side of impeller under part-load conditions, and thus reduced the pressure fluctuation in vaneless region.

For the centrifugal pump with vaned diffuser, scholars also made a lot of attempts at its performance optimization[20-21]. The optimization methods mainly included the direct modification of hydraulic components and applications of intelligent optimization algorithms. Khoeini et al.[22] enhanced the performance of centrifugal pumps by using different angular diffusers. They conducted a simulation study on different vaned and non-vaned with three different wall divergence angles. The main results showed that the vaned diffuser wall divergence angle of 10° could effectively increase the pump head and efficiency under over-load conditions. Meanwhile, the pump performance was significantly improved when the vaned diffuser wall divergence angle was 10° compared with wall divergence angle was 0°. Shi et al.[23] applied the tandem-blade design method in compressors for centrifugal pumps to improve pump performance. The found that the adoption of tandem-blade design improved the jet-wake structure and uniformity of pressure and velocity distributions at impeller outlet. Consequently, the pump was made to have higher performance under a wider operating range. Wang et al.[24] optimized the vaned diffuser of HVCP. Firstly, the influence degree of diffuser design parameters on efficiency was determined by using orthogonal tests, and then the optimal combination of diffuser parameters was obtained by using the combination of response surface and multi-island genetic algorithm. The efficiency of optimized centrifugal pump was improved by 8.65%.

It is evident from previous studies that the matching of hydraulic components has a large impact on the performance of HVCP. Some methods to optimize the performance of HVCP were proposed, but the understanding of performance variation mechanism and reasons is not sufficient. Hence, this study presents a detailed comparative analysis of the energy loss and flow patterns of two HVCP models, focusing on the hydraulic component matching to reveal the performance improvement mechanism. This study will be more helpful to achieve a more efficient and energy-saving design for following HVCP.

1. Numerical methods and calculation model

1.1 Calculation model

Figure 1 shows a HVCP model ($n_s = 215$) with one-layer stay vane for simulation analysis. The stay vane in HVCP plays an important role in controlling flow patterns and balancing radial forces. The key parameters of HVCP model are listed in Table 1. All the hydraulic components including elbow inlet pipe, centrifugal impeller, vaned diffuser and volute were first modeled individually by 3-D software and then the assembly was completed. The elbow inlet pipe and outlet pipe of volute were properly extended to ensure the uniformity of inlet and outlet flow, which were also coincided with experimental devices.

1.2 *Grid division*

ANSYS preprocessor ICEM CFD was utilized to grid four calculation domains (inlet pipe, impeller, stay vane and volute) individually with hexahedral structure, and then assembled to obtain the overall calculation domain as shown in Fig. 2. Since the quality of grid is crucial to the accuracy of simulation results, the O-block grid was applied for the calculation domain of inlet and volute extension pipes. For symmetric hydraulic components with blades (impeller and vaned diffuser), a more complex J/O grid

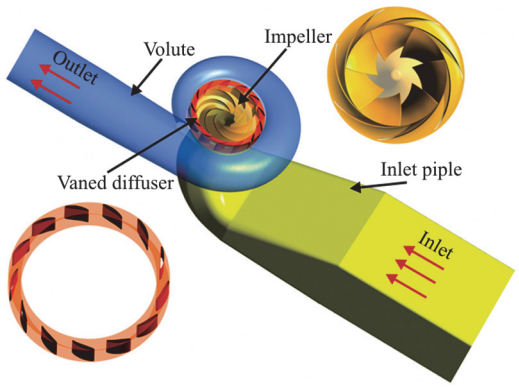

Fig. 1 (Color online) Calculation model of HVCP

Table 1 Basic design parameters of HVCP

Parameter	Value
Design flow rate, Q_{des} /($m^3 \cdot s^{-1}$)	0.214
Design head, H_d /m	18.74
Rotational speed, n /($r \cdot min^{-1}$)	1 150
Specific speed, n_s	215
Impeller inlet diameter, D_j /mm	274.1
Impeller outlet diameter, D_2 /mm	360
Number of impeller blades, Z	7
Number of stay vanes, Z_s	13

was used to first divide individual blade channel, and finally the overall grid was obtained by the periodic array grid method. For volute domain grid division, a combination of multiple topologies was chosen due to the volute tongue structure. Considering that the flow separation and vortices were easily occurred near wall surfaces of impeller blades and stay vanes, the local grid refinement was conducted for boundary layers. These grid division details are also shown in Fig. 2.

1.3 *Turbulence model and boundary conditions*

When the Reynolds-averaged Navier-Stokes (RANS) method was used for simulations, the turbulence model should be applied. The prediction of turbulence details in the pump is widely varied by using different turbulence models. The characteristics of HVCP determine the greater variations of turbulence intensity in circumferential direction of impeller. Meanwhile, the near wall surfaces of impeller blades and diffuser vanes are easily producing shear flow and flow separations. The shear stress transport (SST) k-ω turbulence model proposed by Menter in 1994[25] was more accurate for the calculation of initiation and intensity of flow separation under adverse pressure gradient. The orthogonal divergence term is also considered in this model, which drives the model to be more applicable at both near and far wall surfaces, so it is very suitable for the calculation at convective adverse pressure regions. In addition, the SST k-ω turbulence model was more widely and successfully applied in previous studies[26-27], so it is chosen for simulations in this study.

The turbulent viscosity μ_t, turbulent kinetic energy k and turbulence frequency ω in SST k-ω

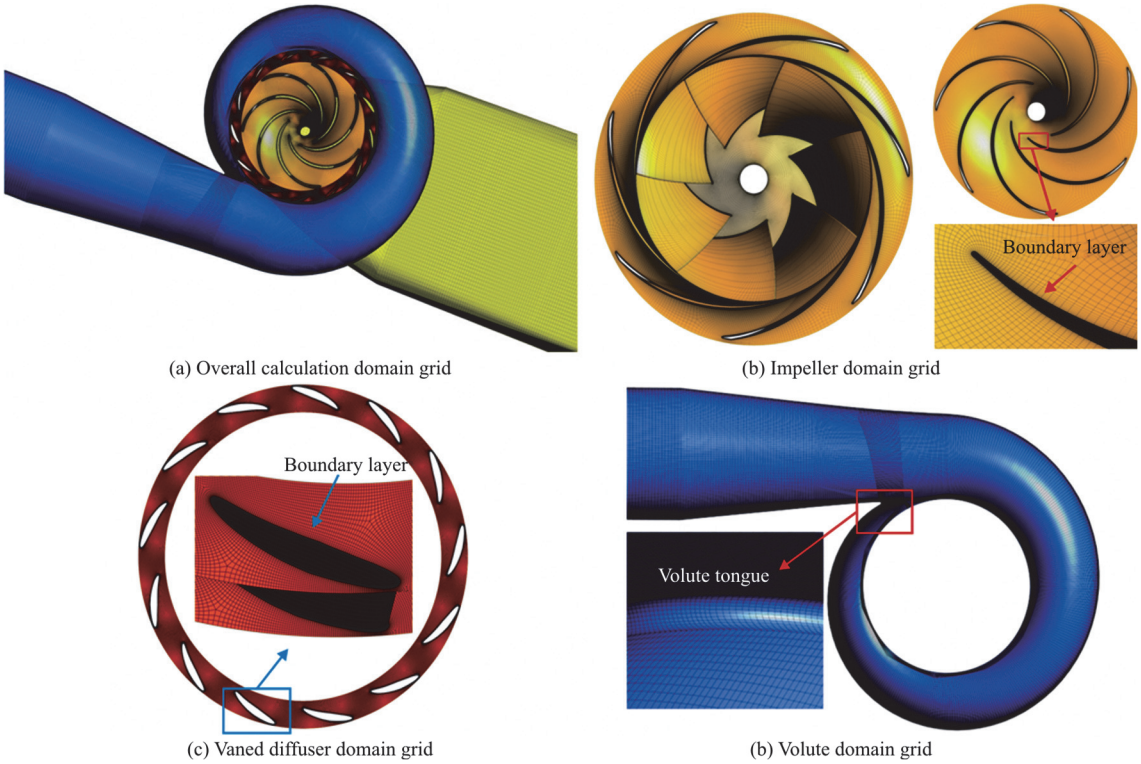

(a) Overall calculation domain grid
(b) Impeller domain grid
(c) Vaned diffuser domain grid
(b) Volute domain grid

Fig. 2 (Color online) Calculation domain grid of HVCP

model are defined as:

$$\mu_t = \frac{\rho a_1 k}{\max(a_1\omega, SF_2)} \tag{1}$$

$$\frac{\partial(\rho k)}{\partial t} + \frac{\partial}{\partial x_j}(\rho u_j k) = P_k - \beta'\rho k\omega + \frac{\partial}{\partial x_j}\left[\left(\mu + \frac{\mu_t}{\sigma_{k2}}\right)\frac{\partial k}{\partial x_j}\right] \tag{2}$$

$$\frac{\partial(\rho\omega)}{\partial t} + \frac{\partial(\rho u_j\omega)}{\partial x_j} = \alpha_2 S^2 - \beta_2\rho\omega^2 + \frac{\partial}{\partial x_j}\left[\left(\mu + \frac{\mu_t}{\sigma_{\omega 2}}\right)\frac{\partial\omega}{\partial x_j}\right] + 2(1-F_1)\frac{\rho\sigma_{\omega 2}}{\omega}\frac{\partial k}{\partial x_j}\frac{\partial\omega}{\partial x_j} \tag{3}$$

where a_1 is put equal to 0.31, F_1, F_2 is the hybrid function to realize the conversion between k-ω, k-ε models and S is the invariant of strain rate. Also add restrictions to the vortex viscosity equation, and defined as

$$\nu_t = \frac{\mu_t}{\rho} \tag{4}$$

In the above equations, a mixed form of internal and external constants is used to represent each constant, which is defined as

$$\varphi = \varphi_1 F_1 + \varphi_2(1-F_1) \tag{5}$$

where φ_1 is the internal constant, φ_2 is the external constant.

The hybrid function is used to establish a connection between the near wall distance and flow variables, which determines whether the SST k-ω turbulence model can be successfully calculated. The mixing and closure functions are defined as:

$$F_2 = \tanh\left[\left[\max\left(\frac{2\sqrt{k}}{\beta'\omega y}, \frac{500\nu}{y^2\omega}\right)\right]^2\right] \tag{6}$$

$$P_k = \min\left(\tau_{ij}\frac{\partial u_i}{\partial x_j}, 10\beta'k\omega\right) \tag{7}$$

$$F_1 = \tanh\left\{\left\{\min\left[\max\left(\frac{\sqrt{k}}{\beta'\omega y}, \frac{500\nu}{y^2\omega}\right), \frac{4\sigma_{\omega 2}k}{CD_{k\omega}y^2}\right]\right\}^4\right\} \tag{8}$$

$$CD_{k\omega} = \max\left(2\rho\sigma_{\omega 2}\frac{1}{\omega}\frac{\partial k}{\partial x_i}\frac{\partial\omega}{\partial x_i}, 10^{-10}\frac{500\nu}{y^2\omega}\right) \tag{9}$$

where ν is the dynamic viscosity.

ANSYS CFX was used for simulations of HVCP. The boundary conditions were set based on the actual operating conditions of HVCP. The total pressure was applied at the inlet of elbow inlet pipe extension, and the value was set to 1 atm. The boundary condition at the outlet of volute extension was set to mass flow rate, which changed with the pump operating conditions and the design condition is 214 kg/s. The impeller domain was set as rotating domain with 1 150 r/min as rotational speed. The roughness of wall surfaces was ignored, so each physical wall was set as no-slip wall. The wall function adopts automatic mode. The grid interface of each calculation domain was connected by GGI, and the interface condition between the rotating and stationary domains was set to be "Frozen Rotor", "Transient Rotor-Stator" for steady and unsteady simulations. The SIMPLEC algorithm was used for pressure-velocity coupling, and the discrete format of convection term was a second-order windward format. The second order backward Euler was used for the transient term. The maximum iteration step for steady simulation was set to 1 500 and the convergence accuracy was set to 10^{-5}. The time step of unsteady simulation is 2.8986×10^{-4} s, which corresponding to 2° of impeller rotation.

1.4 *Grid independence test*

It is essential to verify the independence of grid nodes number with simulation results. The same grid topology was applied to each case, and only the number of grid nodes was changed. Seven groups of grid schemes were set up for independence test and the pump performance parameters were obtained, i.e., head H, efficiency η, as shown in Fig. 3.

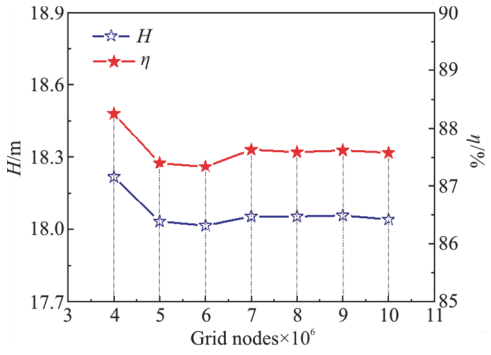

Fig. 3 (Color online) Comparison of the performance parameters under different grid nodes

When the grid nodes number is increased to 7×10^6, the fluctuations of H, η is less than 1%, which means it meets the grid independent test requirement. However, an excessive number of grid nodes can lead to an increase in calculation time and resource wastage. Hence, 7×10^6 grid nodes were selected for final calculation. The specific grid information of each hydraulic component is listed in Table 2. In

Table 2 Grid information of each calculation domain

Domain	Number of elements	Number of nodes	Average y^+ of blades/vanes
Inlet pipe extension	636 150	653 528	-
Inlet pipe	691 310	711 480	-
Impeller	1 743 588	1 826 265	4.24
Vaned diffuser	1 675 624	1 780 720	4.91
Volute	2 043 733	2 157 662	-
Total	6 790 405	7 129 655	-

particular, the average y^+ value for impeller blades and diffuser vanes are 4.24, 4.91.

1.5 *Optimization of the calculation model*

The original calculation model in Section 1.1 is defined as model A. In order to reduce the energy consumption of HVCP as much as possible, model A was optimized with the objective of maximum efficiency under design condition. The vaned diffuser and volute were the main objects of optimization. This was in consideration of the key location of vaned diffuser in HVCP and hydraulic components matching. The specific optimization design process was shown in Fig. 4. The sensitivity analysis of the optimized parameters was completed by using the Plackett-Burman method. Four key design parameters of the vaned diffuser and volute that have a significant impact on the efficiency, i.e., diffuser inlet diameter D_3, diffuser inlet vane angle β_3, volute channel inlet width b_4 and volute throat area S_B were defined as optimization variables. An automatic numerical simulation optimization platform was built by Isight to calculate 106 sets of samples. High-precision relationships between optimization variables and objective were established based on sample data and artificial neural network (ANN). Finally, the optimization design was completed based on ANN and particle swarm algorithm (PSO). The more details of optimization design process were described in Ref. [28]. And the optimized model is defined as model B. The comparison of design parameters between models A, B is listed in Table 3. Compared with model A, D_3, β_3 and b_4 of model B are increased, while S_B is decreased, i.e., each section of model B volute is narrowed. A comparison of the vaned diffuser and volute domains for models A, B is shown in Fig. 5.

2. Experimental measurement and verification

The performance experimental measurements of model B were completed. The experiment was carried out on the closed experiment loop of vertical centrifugal pump. The basic layout and details of experiment loop are shown in Fig. 6. The experiment loop is mainly composed of valves, water tanks, test pump, motor, torque meter, electromagnetic flow meter and pressure sensors etc. The performance parameters of test pump were measured under multiple operating conditions, where the effect of cavitation was ignored. Allow the motor to idle before connecting to the pump shaft to eliminate additional torque. The H was calculated based on the pressure sensors at test pump inlet and outlet regions, while the η was calculated from the flow rate Q, H and torque, as defined in Eq. (10).

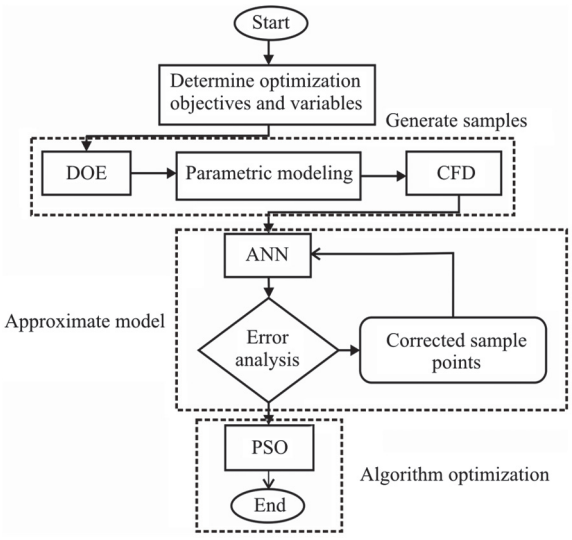

Fig. 4 The optimization procedure of the vaned diffuser and volute

$$\eta = \frac{P_e}{P} \times 100\%, \quad P_e = \frac{\rho g Q H}{1\,000} \tag{10}$$

where P indicates the input power of the pump, P_e is the output power of the pump.

The experiment loop facility and experiment equipment used in this paper has the identification from the technology department of Jiangsu Province. The range and accuracy of the measuring instrument are shown in Table 4. The comprehensive uncertainty U of the experiment includes random uncertainty

Table 3 Comparison of parameters between models A, B

Design parameters/unit	D_3 /mm	β_3 /°	b_4 /mm	S_8 /mm^2	η_d /%	H /m
Model A	379.8	27.0	118.0	50 650	87.60	18.07
Model B	389.6	30.2	131.6	41 896	90.82	19.11

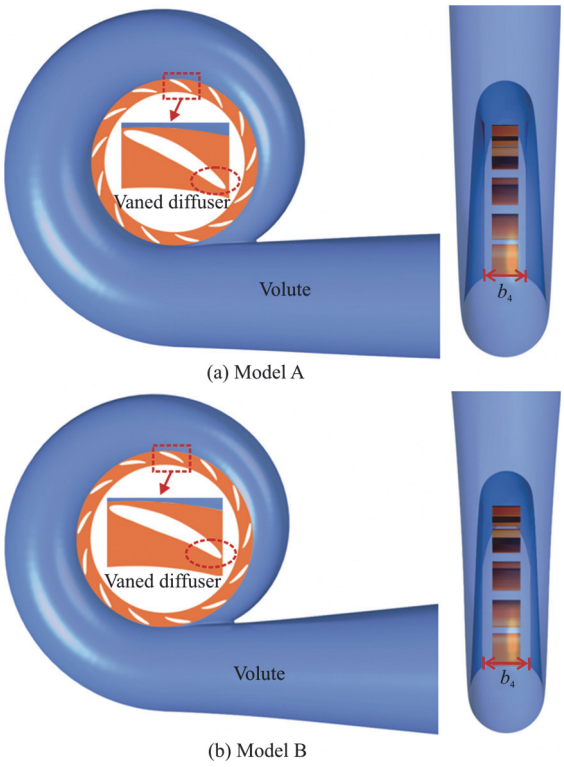

Fig. 5 (Color online) Compairson of hydraulic models between models A, B

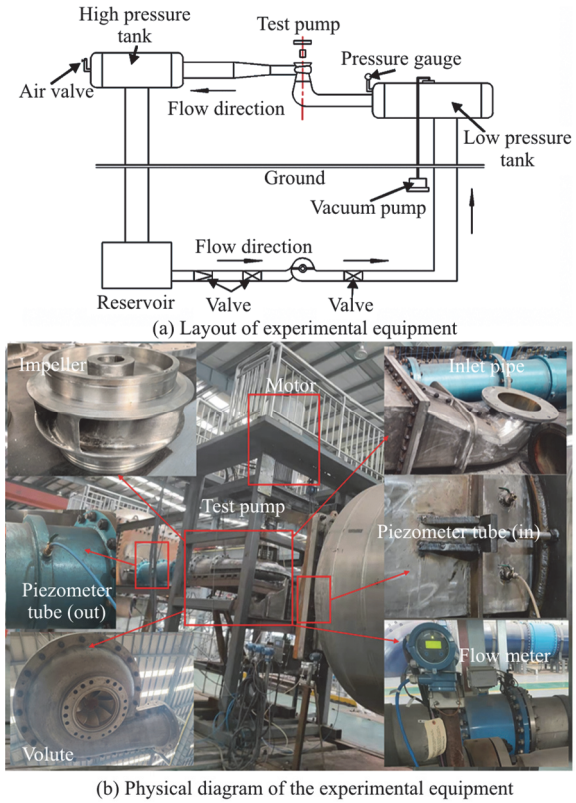

Fig. 6 (Color online) Physical diagram of experiment equipment

U_{sto} and system uncertainty U_{sys}. The measurement data Q, H and n are collected repeatedly for 6 times under a certain pump condition, and the stard T-type distribution was used to calculate the U_{sto}. The system uncertainty U_{sys} analysis part is determined by the methods and accuracy of measuring instruments. The U of each component is to be calculated by the square root of the sum of the squares of the U_{sto}, U_{sys}. The specific calculation results are shown in Table 5. The overall uncertainty U_{all} of performance measurement of this experiment is 0.35%.

The η, H were also obtained from the steady simulation (CFD) of model B under multiple operating conditions and compared with the experimental data, as shown in Fig. 7. The relative error was calculated by Eq. (11). Figure 7(a) shows that the CFD calculations of η, H are in good agreement with EXP. The η reaches a maximum value under design condition and decreases sharply under part-load conditions. The CFD η is always higher than experimental. The H decreases continuously as the increased flow rate. In Fig. 7(b), the errors in η are all less than 5% and the differences in errors are small

Table 4 Range and accuracy of measurement apparatus

Apparatus	Type	Type	Range	Accuracy
Electromagnetic flowmeter	1700R12ABZMZZZ	Flow rate, Q /(m^3·h^{-1})	0-2 592	±0.05%
Pressure Transmitters	3051TA1A2B21A	Pressure, p /MPa	–0.1-0.3	±0.04%
Dynamometer and speed sensor	TQ-660	Torque, M /(N·m)	0-3 000	±0.10%
-	-	Rotational speed, n / (r·min^{-1})	0-30 000	±0.10%

under each operating condition. The maximum error is 3.9% under over-load conditions. The errors of H are increased under part-load and over-load conditions, with a maximum error of 6%. Under part-load conditions, the CFD H are lower than experimental, while the CFD H exceed experimental under over-load conditions.

Table 5 Calculation procedure of experimental uncertainties

Notation	Q /(kg·s^{-1})	H /m	n / (r·min^{-1})
Sample 1	213.98	19.11	1 149.87
Sample 2	214.89	18.46	1 150.11
Sample 3	214.27	18.67	1 150.36
Sample 4	214.36	18.37	1 149.69
Sample 5	215.24	18.17	1 150.23
Sample 6	213.78	19.32	1 150.73
Average value	214.42	18.68	1 150.17
Standard deviation	0.5038	0.4081	0.3359
U_{sto} /%	0.2253	0.1825	0.1502
U_{sys} /%	0.0500	0.0400	0.1000
Components, U /%	0.2308	0.1868	0.1805
Overall uncertainty, U_{all} /%	0.3475	-	-

The clearance leakage losses, disc friction losses and mechanical losses in the experimental test resulted in lower η, H than CFD results. However, the unstable flow patterns in HVCP increase sharply under part-load conditions, such as backflow, secondary flow and flow separation. The SST k-ω model predicts these unstable phenomena beyond the actual range. Thus, the CFD H are lower than experimental under these conditions. It is concluded that the simulation methodology in current study is available to analyze the performance and flow patterns of the high-power vertical centrifugal pump.

$$\gamma = \frac{\phi_{CFD} - \phi_{EXP}}{\phi_{EXP}} \times 100\% \tag{11}$$

3. Results and discussions

3.1 *Performance parameters variation in HVCP*

The comparison of performance parameters between models A, B is given in Fig. 8. The curves of

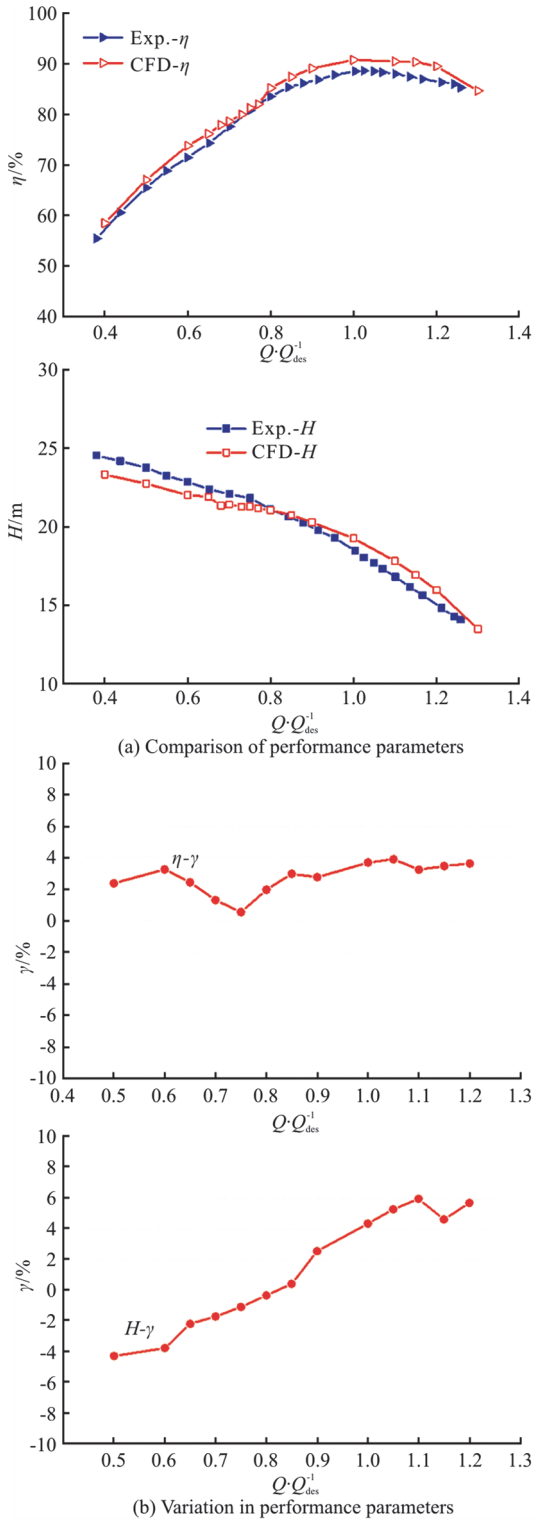

Fig. 7 (Color online) Comparison of simulations and experimental results

η, H are smoothed by the Bessel method. Figure 8(a) shows the η first increases gradually and then decreases as the increased flow rate. The highest η

for model B appears under design condition, while model A appears under over-load condition. The η of model B is significantly higher than model A under design and part-load conditions, but is reversed under over-load conditions. The distributions of efficiency deviation $\Delta\eta$ between models B, A are given in Fig. 8(b). The $\Delta\eta$ is positive under design and part-load conditions with less variable, and $\Delta\eta$ approximately equal to 3%. The maximum $\Delta\eta$ occurs under $0.6Q_{\text{des}}$. The $\Delta\eta$ under part-load conditions shows fluctuations, which is caused by the unstable flow pattern in HVCP. When the flow rates are greater than design condition, the $\Delta\eta$ decreases rapidly and then model B η is lower than model A.

As in Fig. 8(a), H decreases as the increased flow rate. For model B, H is higher than model A except under over-load conditions. The distributions of head deviation ΔH between models B, A is shown in Fig. 8(b). The ΔH always remain positive under $0.4Q_{\text{des}}$-$1.2Q_{\text{des}}$, with the maximum ΔH under $0.5Q_{\text{des}}$. However, under $0.6Q_{\text{des}}$-$0.8Q_{\text{des}}$, the ΔH fluctuates significantly, which is due to the hump characteristic of Q-H curve caused by stall.

Consequently, the performance of model B is significantly improved under design and part-load conditions. The maximum $\Delta\eta$, ΔH are both found under part-load conditions. Meanwhile, model B improves the problem that the maximum η of model A is biased towards over-load conditions. All these phenomena can show that the vaned diffuser and volute also have an important impact on performance of HVCP.

3.2 *Energy loss variation in HVCP*

The variations in performance parameters are closely related to the energy loss in HVCP. Consequently, a detailed comparative analysis of the energy loss in models A, B was carried out based on the energy balance equation. The energy balance equation was first derived from the Navier-Stokes equations by Wilhelm et al.[29]. For incompressible flow without temperature variation, the energy balance equation[30-31] is defined by Eq. (12).

$$P_{\text{LE}} = -\iiint_V \frac{\partial(-\overline{u_i}\,\overline{\rho u_i' u_j'})}{\partial x_j}\mathrm{d}V + \iiint_V \mu \frac{\partial(-\overline{u_i}\,\overline{D_{ij}})}{\partial x_j}\mathrm{d}V + \iiint_V (-\overline{\rho u_i' u_j'})\frac{\partial \overline{u_i}}{\partial x_j}\mathrm{d}V + \iiint_V \mu \overline{D_{ij}}\frac{\partial \overline{u_i}}{\partial x_j}\mathrm{d}V \tag{12}$$

where the strain rate tensor D_{ij} is defined by Eq. (13) and Reynolds stresses $-\overline{\rho u_i' u_j'}$ can be calculated by Eq. (14). The μ_t is modeled based on SST k-ω turbulence model, as defined in Eq. (1).

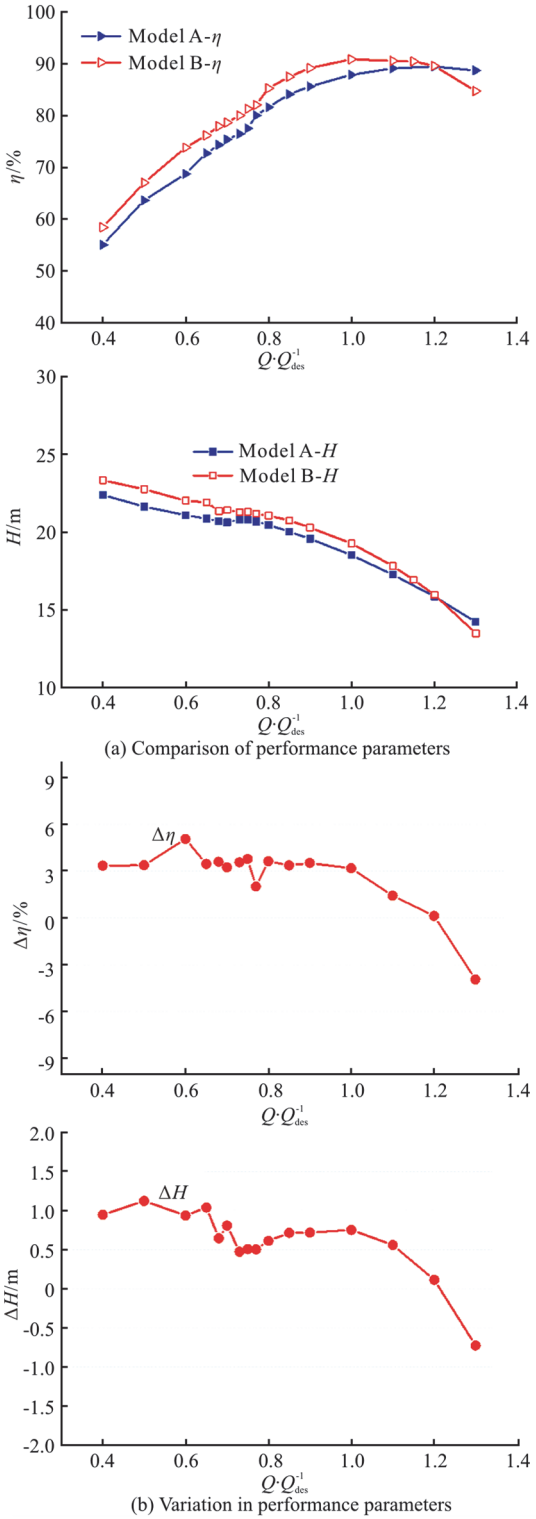

Fig. 8 (Color online) Comparison of the performance parameters between models A, B

$$D_{ij} = \frac{\partial u_i}{\partial x_j} + \frac{\partial u_j}{\partial x_i} \tag{13}$$

$$-\overline{\rho u_i' u_j'} = \mu_t \left(\frac{\partial \overline{u_i}}{\partial x_j} + \frac{\partial \overline{u_j}}{\partial x_i} \right) - \frac{2}{3} \delta_{ij} \rho k \tag{14}$$

The four terms on the right side of the energy balance equation in Eq. (12) are named as P_{L1} - P_{L4}. The P_{L1}, P_{L2} are the Reynolds stress transportation term and viscosity transportation term, which represent the diffusion of kinetic energy through Reynolds stress and viscous stress, respectively. The P_{L3} is the turbulent kinetic energy production term, which represents the transfer of mean kinetic energy to the turbulent kinetic energy. The P_{L4} is named the viscosity dissipation term and denotes the viscous dissipation of mean kinetic energy.

The friction loss caused by strong wall effect is also an important part of the energy loss in HVCP. The terms in Eq. (12) ignore the effect caused by the velocity gradient near the wall regions. Thus, the friction loss near the wall of HVCP is calculated by Eq. (15) based on Refs. [32-33]. And the total energy loss in HVCP is defined by Eq. (16).

$$P_{LW} = \int_A (\boldsymbol{\tau} \cdot \boldsymbol{v}) \mathrm{d}A \tag{15}$$

$$P_L = P_{LE} + P_{LW} \tag{16}$$

where $\boldsymbol{\tau}$ is the wall shear stress, A is the wall area and $\boldsymbol{v}$ is the velocity vector near the center of the first layer of the wall mesh.

The energy loss P_L in each hydraulic component is counted and the P_L in models A, B under design condition is shown in Fig. 9(a). In model A, the maximum P_L is shown in the volute, followed by the impeller and diffuser. The volute domain causes great energy dissipation due to its large volume and strong diffusion flow. While in model B, a significant decrease in P_L occurs in both the volute and diffuser. The P_L in model B volute is close to the impeller. Meanwhile, the P_L in the diffuser is much lower than the impeller and only higher than the inlet pipe in model B. The P_L in the inlet pipe is always small and can be ignored.

Figures 9(b), 9(c) shows P_L in the diffuser and volute of models A, B under different conditions. The P_L in the both model diffusers increases sharply as the decreased flow rate, especially in the model A where P_L increases more rapidly. Under $0.7Q_{des}$ - $1.2Q_{des}$, P_L in the model B diffuser is both reduced compared with model A. The reductions in P_L under part-load conditions are greater than over-load conditions. The comparison of P_L distribution in the volute shows that the P_L of model A is minimal under over-load conditions while model B has minimal P_L under design condition. This corresponds to the high efficiency point of model A appearing under over-load conditions. The P_L in the volute grows rapidly as the decreased flow rate and reaches the maximum value under part-load conditions. The P_L in model B volute is lower than that of model A except under over-load conditions. The greatest P_L reduction is near the design condition.

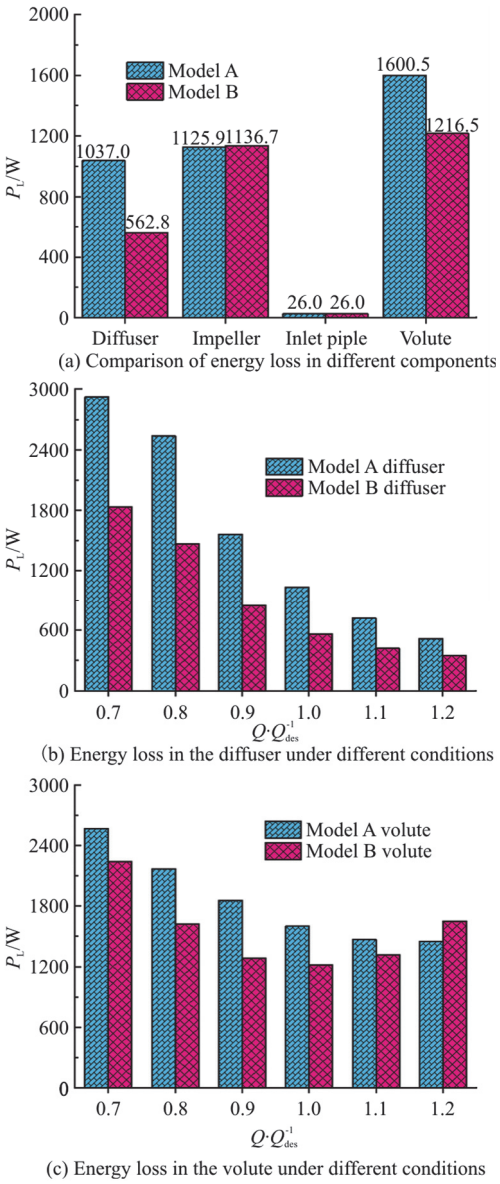

Fig. 9 (Color online) Comparison of energy loss in HVCP

It can be concluded that the characteristics of P_L distribution under multiple operating conditions are in good agreement with the performance parameters variation. The significant reductions of P_L in the diffuser and volute are the main reason for pump performance improvement, especially under part-load conditions.

3.3 *Comparison analysis of energy loss and flow patterns in the diffuser*

The magnitudes of five energy loss terms in models A, B diffuser under different conditions are shown in Fig. 10. The P_{L3} is dominant in the diffuser of both models under all conditions and has the greatest proportion under part-load conditions. From each term distribution under different conditions, the P_{L3}, P_{L1} in the diffuser of both models are increased as the decreased flow rate, and the lower the flow rate, the faster the increase. The P_{L2}, P_{L4} always remain small values. The P_{LW} (energy loss of walls) is second only to P_{L3} but is influenced less by conditions. The comparison of model A and B shows that the P_{L3} in the model B diffuser is smaller than that in model A from $0.7Q_{des}$ to $1.2Q_{des}$, and the P_{L3} in model B is reduced more under part-load conditions. Therefore, the distribution characteristics of P_{L3} in the two models diffusers are highly consistent with those of P_L in Fig. 9(b). The P_{LW} of model B diffuser is also slightly reduced under all conditions compared with model A. The P_{L1} of model B diffuser is also reduced compared with model A under part-load conditions. It can be concluded that the generation of turbulent kinetic energy is the main contribution for the energy loss in the diffuser, followed by the friction loss near the wall. The kinetic energy in the diffuser is converted more into turbulent energy under part-load conditions. The kinetic energy diffusion and wall effects in the diffuser caused by turbulent flow in a high Reynolds number with high velocity gradient cannot be neglected, especially under part-load conditions. The dramatic reduction in the conversion of kinetic energy to turbulent energy in the model B diffuser is one of the key reasons for the pump performance improvement.

Considering that P_{L3} has the greatest effect on the energy loss variation in the diffuser. The specific location and variations for the high P_{L3} in the models A and B diffuser were analyzed in detail. In Fig. 11, different diffuser vane spans 0.1, 0.5 and 0.9 are given at the section near shroud, middle and hub, respectively. The P_{L3}, velocity and streamline distributions of models A, B diffuser at different spans under design condition are shown in Fig. 12.

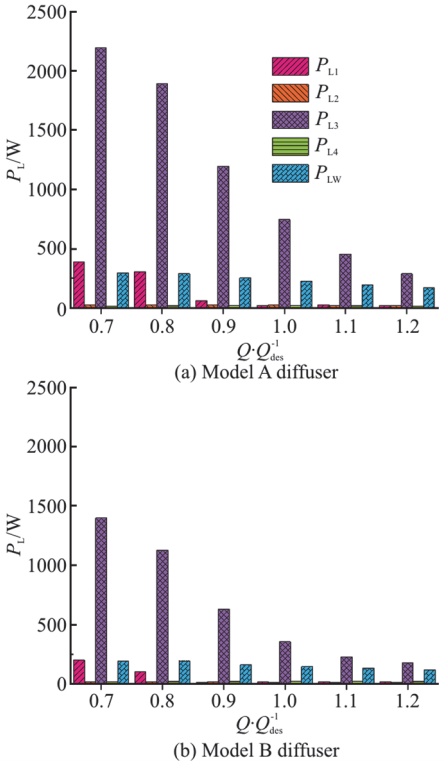

Fig. 10 (Color online) Comparison of each energy loss component in the diffuser

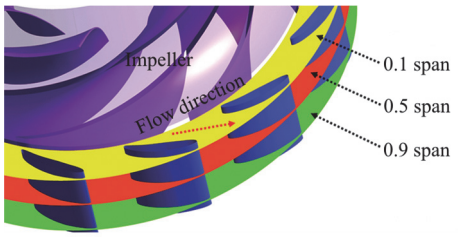

Fig. 11 (Color online) Schematic diagram of diffuser different spans

Figure 12(a) shows the P_{L3} distribution in the model A diffuser with high P_{L3} regions in many channels, as shown in the red frames. The distribution of high P_{L3} regions in the diffuser is usually at intervals. Also, the distribution of P_{L3} at different spans shows significant differences. The high P_{L3} regions are the most abundant at 0.5 span and the least at 0.9 span. The high P_{L3} regions in the model B diffuser are significantly reduced in Fig. 12(b). The P_{L3} at the same location is significantly reduced compared with model A, as shown in the red frames. Especially at 0.5 span, high P_{L3} regions can be rarely

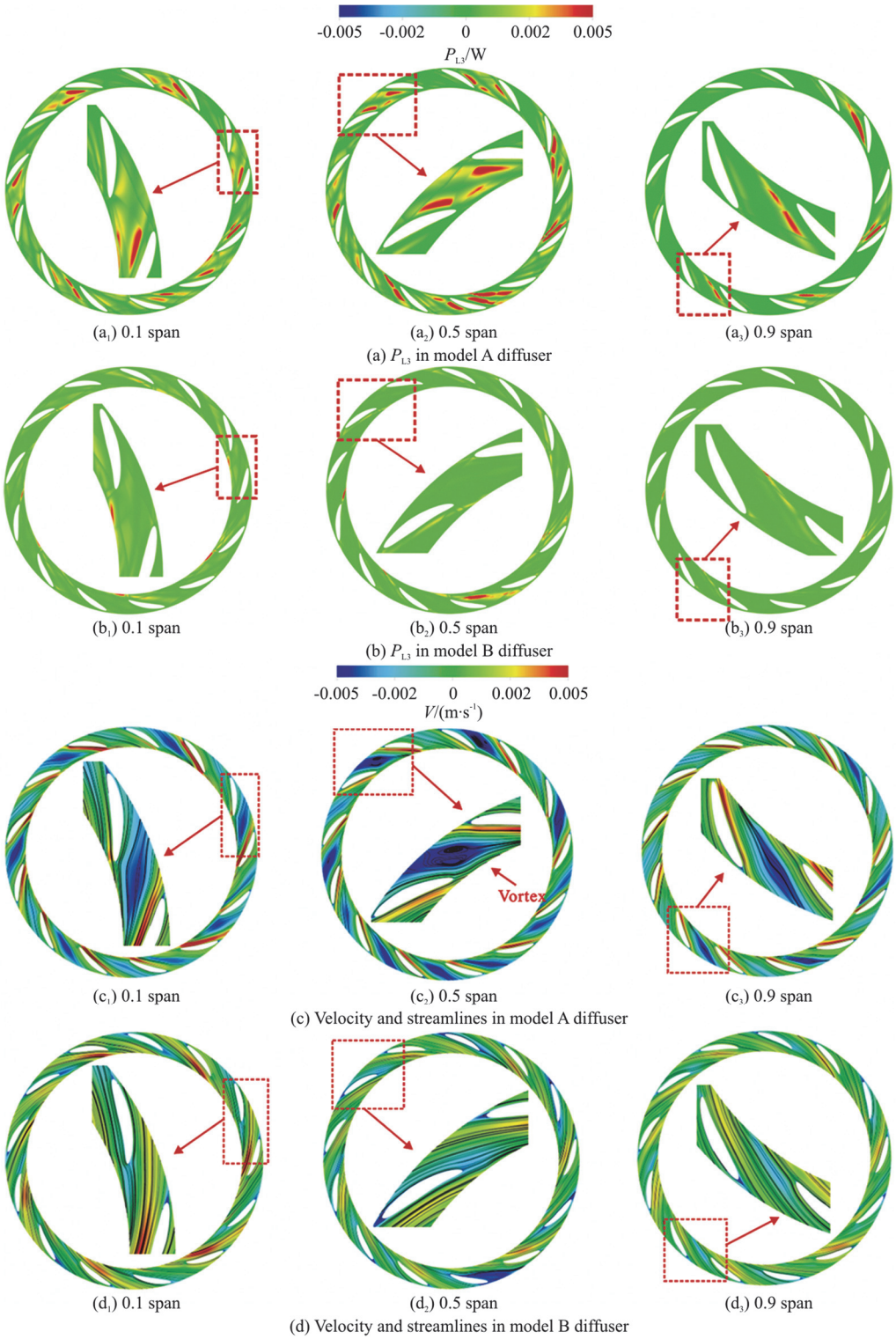

Fig. 12 (Color online) P_{L3} velocity and streamlines distributions of vaned diffuser at different spans

observed in the diffuser channels. Therefore, the turbulence loss in the model B diffuser flow channel is greatly reduced.

The velocity and streamline distributions in Figs. 12(c), 12(d) can be used to better compare the flow pattern variation in the diffuser and to explain the generation of high P_{L3} regions. Figure 12(c) shows the velocity distribution in model A diffuser is not uniform and large low-velocity regions exist in several channels. The locations of these low-velocity regions are highly coincident with the high P_{L3} regions in Fig. 12(a). In the red frames, the clear vortices are

shown in low-velocity regions at 0.5 span and cause flow channel blockage. The streamlines in low-velocity regions at 0.1 span, 0.9 span are also clearly curved. The mismatch between model A impeller outlet flow angle and β_3 results in serious flow separation in diffuser channels. Especially, vortices are formed at 0.5 span and cause great ow-velocity regions. And these vortices force the fluid to flow into adjacent channels or other spans. This causes uneven flow around the circumferential and axial directions in the diffuser. The vortex and uneven flow patterns in the diffuser are important reasons for the high P_{L3}.

As shown in the red frames in Fig. 12(d), low-velocity regions in the model B diffuser channels are largely disappeared and the streamlines are smoothly uniform. The flow patterns at different channels and spans of vaned diffuser are remained stable. Corresponding to the P_{L3} in Fig. 12(b) is consistently low at different spans. The D_3, β_3 of model B are increased, so that the flow angle at impeller outlet can be better matched to β_3. The improved velocity and streamline distributions in the circumferential and axial directions are an important sign of this better matching. As a result, the turbulence loss in the vaned diffuser are greatly reduced.

The velocity decomposition in HVCP is shown in Fig. 13. The absolute velocity V can be decomposed into circumferential velocity V_t and meridional velocity V_m. Simultaneously, the V_m can be split into two velocities in the radius and axial directions V_r, V_a. The value of V_m reflects the over-flow capacity at local position. Hence, V_m is used for quantitative analysis to further identify the flow pattern variation in vaned diffuser. The V_m distributions of models A, B diffusers from inlet to outlet and from shroud to hub are shown in Fig. 14. The definition of location parameters is shown in Fig. 14(a). The V_m values at the locations shown in Fig. 14(a) were read in all 13 vaned diffuser channels. And the analysis was also performed based on the average value of V_m at the same location in each flow channel.

In Fig. 14(b), the V_m at model A diffuser inlet is below 2m/s under all conditions. The V_m from hub to shroud is stable under $1.2Q_{des}$, indicating that the flow pattern along the axial direction is superior. Under $1.0Q_{des}$, the minimum value of V_m appears at 0.8 span, indicating that the over-flow capacity is decreased near shroud. The fluctuation of V_m from hub to shroud increases under $0.8Q_{des}$ and the minimum value of V_m appears at 0.2 span, so the flow is more unstable. Under $1.2Q_{des}$, the V_m of model B increases slightly compared witht model A. Under $1.0Q_{des}$, the V_m of model B increases significantly compared with model A, especially at 0 span-0.5 span location. Hence, the over-flow capacity at model B diffuser inlet is significantly improved. Under $0.8Q_{des}$, the V_m of model B increases more from middle to shroud, but the V_m is still small near hub.

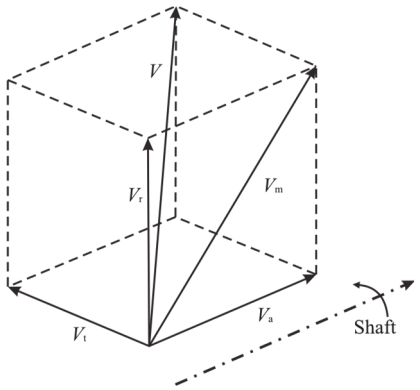

Fig. 13 Decomposition of velocity in the pump

As seen in Fig. 14(c), the distinction in V_m of two models is evident in diffuser middle. Under $1.2Q_{des}$, the V_m is significantly reduced at 0.8 span. The V_m of model B is increased than model A. The flow pattern at diffuser middle is already stable under over-load conditions, so the improvement is not remarkable. Under $1.0Q_{des}$, the V_m of model A from middle to shroud is below 0.5 m/s. Corresponding to Fig. 12, this is due to the vortex existing in the flow channel, which disappear near hub and then the V_m increases. The V_m of model B increases significantly and distributes very uniform under $1.0Q_{des}$. From Fig. 14(b), this is due to the increased V_m at diffuser inlet resulting in the over-flow capacity also significant increases at diffuser middle. Under $0.8Q_{des}$, the V_m at diffuser middle of model A remains consistently low. The V_m of model B is improved considerably, especially near shroud.

In Fig. 14(d), the V_m distribution patterns at diffuser outlet under three conditions are basically the same as that of diffuser middle. The V_m of model B diffuser both increases under three conditions, with the most pronounced increase and uniform distribution under $1.0Q_{des}$. The V_m of model B increases significantly than model A under $0.8Q_{des}$ but the V_m

difference between the hub and shroud is also increased. This indicates a strong axial flow appears in the vaned diffuser.

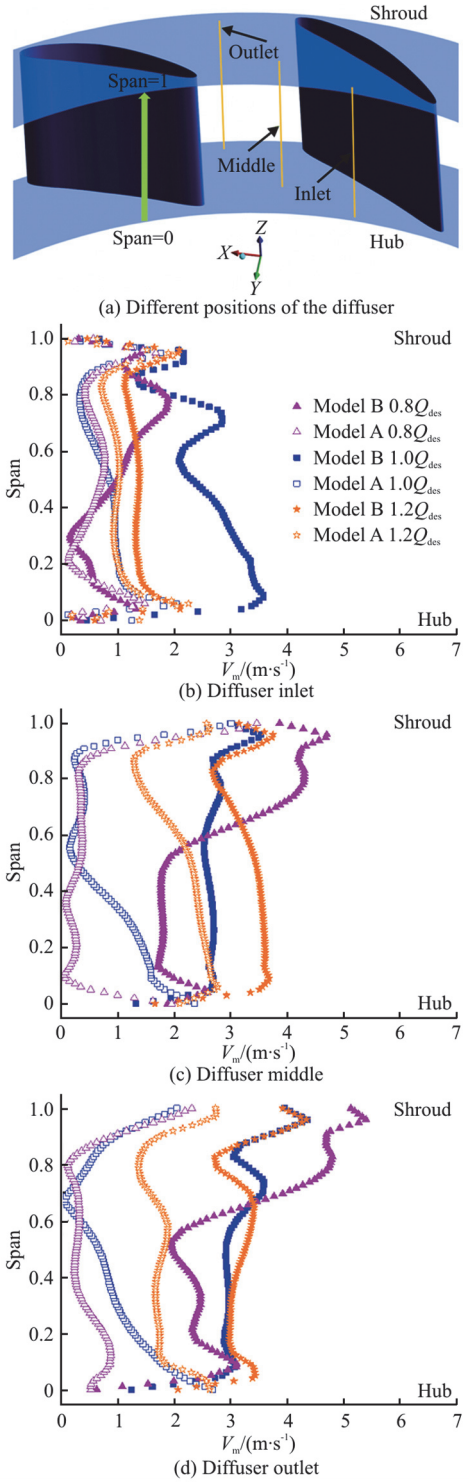

Fig. 14 (Color online) Meridional velocity distribution in the vaned diffuser

The increased V_m is mostly noticeable at diffuser middle, shroud under design and part-load conditions. Consequently, the diffuser over-flow capacity increases more and energy loss reduces more under design and part-load conditions. Moreover, the increased over-flow capacity at diffuser inlet is an important reason for the increased over-flow capacity at the diffuser middle and outlet. The key factor in the energy loss reduction of model B is due to the optimized matching between impeller and vaned diffuser. This matching optimization is even more evident for the HVCP performance improvement under part-load conditions.

A quantitative analysis of pressure distribution in models A, B vaned diffusers was carried out to show the variation in pressure expansion capacity. The static pressure coefficient C_{sp} in this study is defined as

$$C_{sp} = \frac{p - p_{ref}}{0.5\rho u_2^2} \tag{17}$$

where p is the static pressure in the diffuser, p_{ref} is the reference pressure, u_2 is the impeller outlet circumferential velocity.

Figure 15 shows the C_{sp} distributions along the diffuser streamline direction under three conditions. As shown in Fig. 15(a), the horizontal coordinate S_v represents dimensionless distance between diffuser inlet and outlet, with 0 represents diffuser inlet, 1 represents diffuser outlet. The vertical coordinate represents surface average of C_{sp} in the circumferential direction. The C_{sp} gradually decreases as the increased flow rate. The C_{sp} tends to rise from inlet to outlet under all conditions, which is in accordance with the diffuser function. The slope of model A C_{sp} curve varies considerably under $0.8Q_{des}$, indicating unstable energy conversion. The C_{sp} curve of model B is smoother, especially at the diffuser middle. It indicates that the uniformity of pressure distribution in the diffuser is improved. However, the C_{sp} in model B is lower than model A. This is due to the improved flow pattern in diffuser channels and thus the C_{sp} reduction caused by increased flow velocity. Under $1.0Q_{des}$, the slope of model A C_{sp} curve varies considerably in the range of $0S_v$ - $0.35S_v$ (vaneless region and the leading edge of vanes). In contrast, model B has a smoother C_{sp} curve in this region and higher C_{sp} than model A, as shown in the red frame. Under $1.2Q_{des}$, the pressure expansion capacity of model A diffuser is

better. This is due to a stable flow pattern, which also corresponds to the highest η of model A is biased towards over-load conditions. While model B shows a C_{sp} drop at diffuser middle, as shown in the green dashed frame. This is due to the local vortices that appear in the diffuser middle channel.

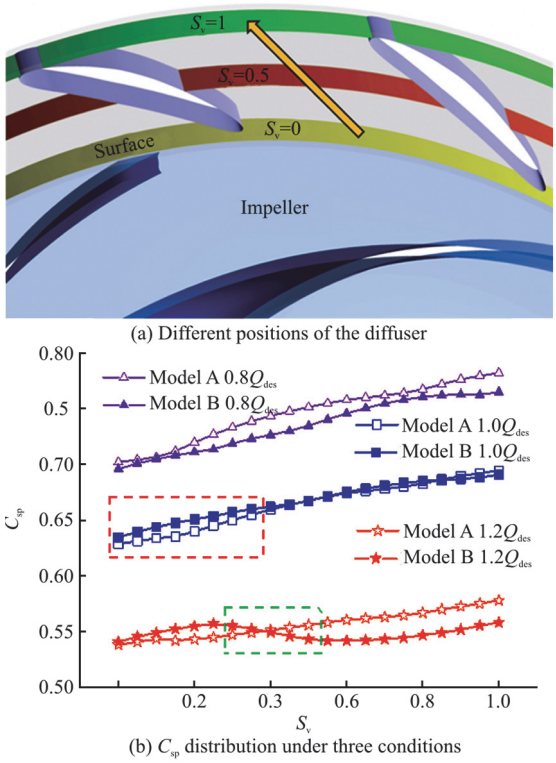

(a) Different positions of the diffuser

(b) C_{sp} distribution under three conditions

Fig. 15 (Color online) C_{sp} distribution in the vaned diffuser

It can be concluded that the pressure expansion capacity of vaned diffuser is optimized under both design and part-load conditions, especially in the vaneless and diffuser inlet regions. This confirms again that the increased D_3, β_3 can greatly optimize the matching between impeller and vaned diffuser. The flow pattern in the diffuser inlet regions is improved.

3.4 *Comparison analysis of energy loss and flow patterns in the volute*

Each term of P_L in the volute are given in Fig. 16. The P_{L3} is always the main contributor to the energy loss in the volute under all conditions. The P_{L2}, P_{L4} are always small and can be ignored in the volute. In the model A volute, the P_{L3} increases as the decreased flow rate. The minimum value of P_{L1} is under design condition and P_{L1} increases gradually when deviating from design condition. The rotational flow in the volute causes friction loss near the wall, so the P_{LW} is also significant. In the model B volute, the P_{L3} is minimal under the design condition and increases more rapidly under part-load conditions. The P_{L1} in the model B volute shows a maximum value under over-load conditions. It indicates that the Reynolds stress transmission in the volute causes greater energy loss under over-load conditions. The P_{L3} in the model B volute is most reduced under design condition compared with model A, which is consistent with Fig. 9(c). The P_{L1} in the model B volute is also decreased under part-load conditions, but increased under over-load conditions. The P_{LW} in the model B volute is slightly higher under several conditions, which is due to the accelerated absolute velocity in the model B volute that results in more friction loss.

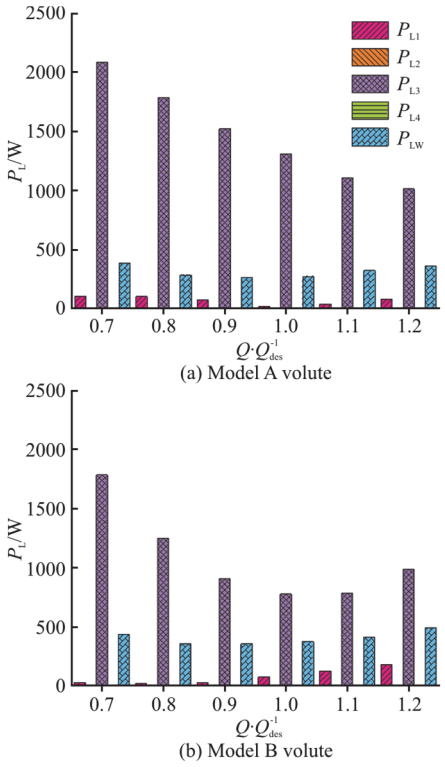

(a) Model A volute

(b) Model B volute

Fig. 16 (Color online) Comparison of each energy loss component in the volute

To provide a more intensive analysis of reasons for the P_{L3} variation in the two model volutes, the distributions of V_t are shown in Fig. 17. As illustrated in Fig. 13, V_t occupies the major component of V in the spiral volute. In Fig. 17(a), V_t in the model A volute remains low and bands of high-velocity regions are appeared under $0.8Q_{des}$.

The magnified figures show that low and negative velocity regions are located in almost each diffuser flow channel and are mostly appeared at suction surfaces of vanes. From streamlines distributions show that the vortex lead to negative values of V_t. The high-velocity regions are observed at pressure surfaces. This is due to the flow blockage at middle of flow channel, forcing the fluid to move near pressure surfaces with high velocity. This high and low V_t distribution characteristic is propagating from the diffuser outlet to volute and results in uneven V_t distribution in the volute. Model B volute has a significantly larger and more uniform distribution of V_t under $0.8Q_{des}$. This is due to V_t in the diffuser is improved significantly, with low and negative velocity regions only in part of channels and not propagating into the volute. In addition, as the decreased volute section area, the flow patterns in the model B volute are better.

In Fig. 17(b), the flow patterns improvement in the model B volute under $1.0Q_{des}$ is essentially the same as that under $0.8Q_{des}$. The V_t distribution in the model B diffuser is significantly improved, with only part low and negative velocity regions appearing at the volute tongue. Figure 17(c) shows a positive V_t distribution in the model A diffuser and volute under $1.2Q_{des}$, and no significant unstable flow phenomena are observed. However, the strong rotor-stator interaction between impeller and volute tongue leads to an uneven V_t distribution in the volute outlet pipe. V_t in the model B diffuser and volute is further increased, but so is the rotor-stator interaction at volute tongue. The large low and negative velocity regions appear at the volute tongue and extend into the outlet pipe. As a result, the flow pattern in the volute is not significantly improved under over-load conditions, i.e., the P_{L3} is also not reduced.

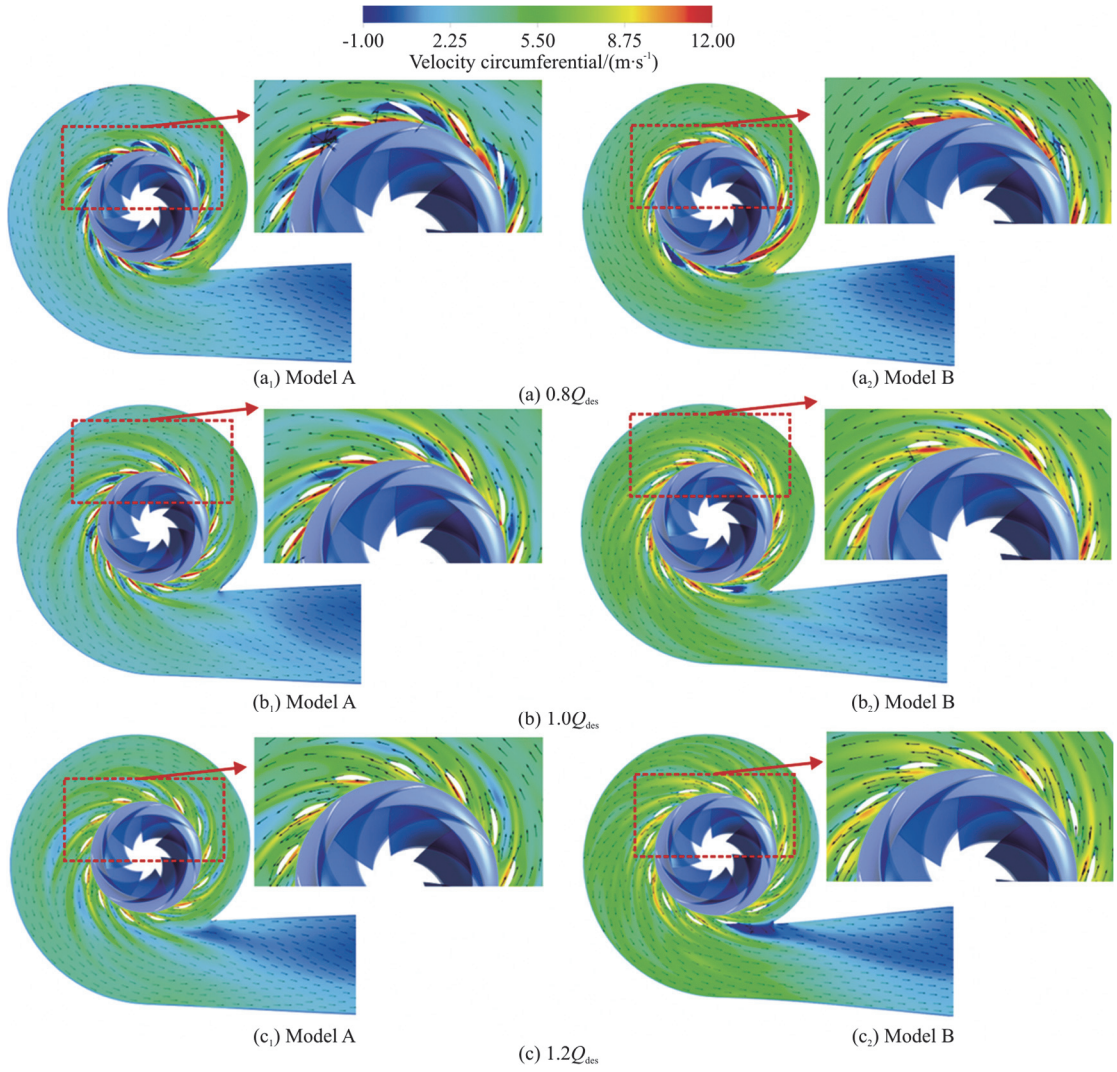

Fig. 17 (Color online) V_t and streamline distributions in the volute

The P_{L3} is used to show the distribution pattern of turbulence loss at different locations in the volute. Figure 18 shows the local P_{L3} distribution contours under three conditions in models A, B volutes. The volute section numbers are shown in Fig. 18(a).

Under $0.8Q_{des}$, the local high P_{L3} regions and an uneven P_{L3} circumferential distribution are shown at the model A volute inlet surface. This is mainly influenced by the unstable flow from the diffuser outlet as shown in Fig. 17. High P_{L3} regions in sections 1-8 spread from the section inlet to middle. The P_{L3} at the model B volute inlet surface is significantly reduced under $0.8Q_{des}$. This is due to the improved flow pattern in the diffuser and results in an increased flow stability at diffuser outlet. As the decreased P_{L3} at inlet surface, the high P_{L3} diffusion phenomenon in each volute section of model B is also significantly weaker, especially in small sections 1-4. It also explains the significant reduction of P_{L3} in model B volute in Fig. 16. In Fig. 18(b),

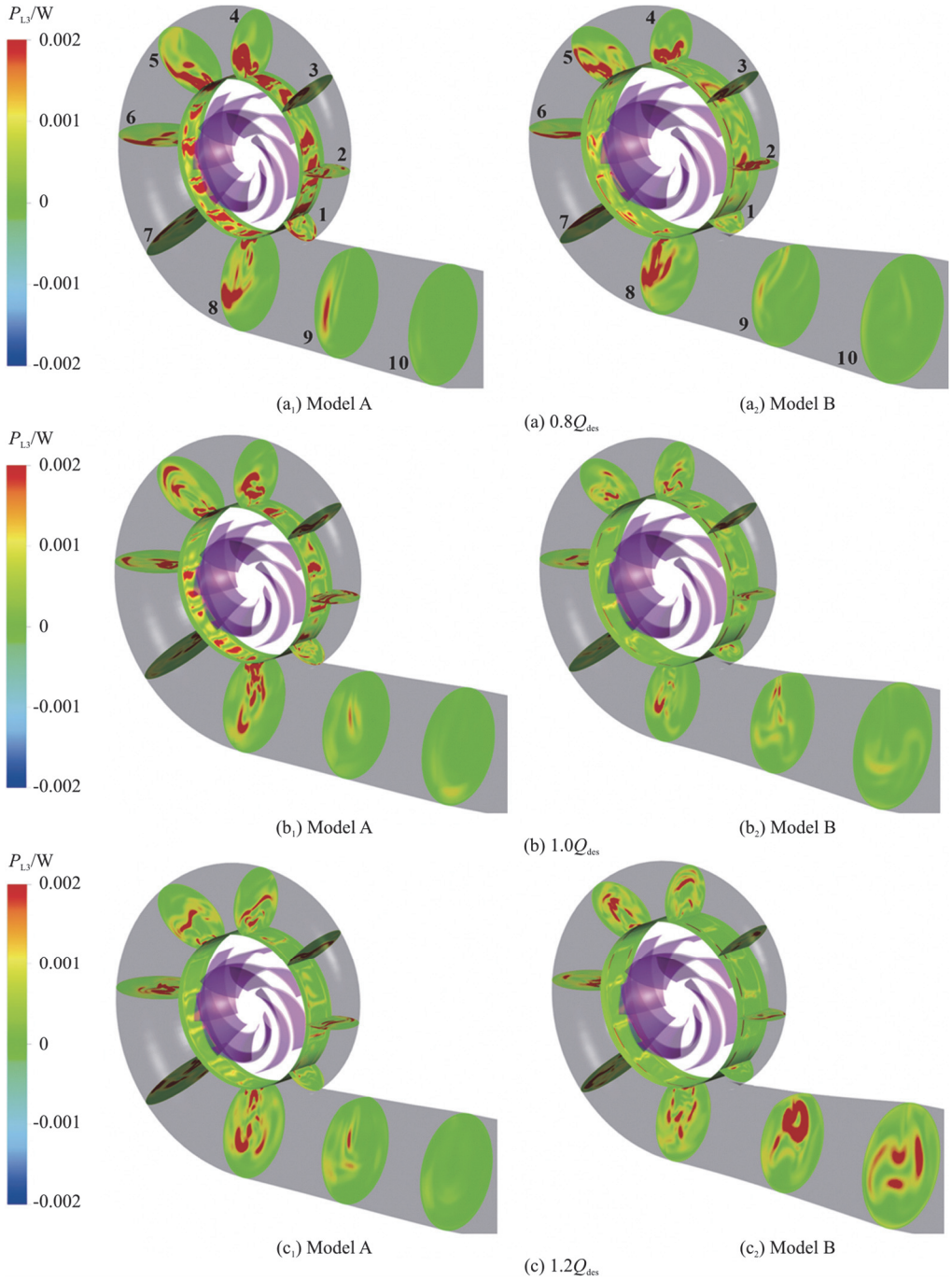

Fig. 18 (Color online) P_{L3} distribution in the volute

the model A volute still has high P_{L3} regions at the inlet surface under design condition, but it is decreased compared with that under $0.8Q_{des}$. Hence, the high P_{L3} regions in each volute section are also reduced. Model B volute has almost no high P_{L3} region at the inlet surface under design condition, resulting in a significant reduction of P_{L3} in each section compared with model A. It indicates that the matching between the diffuser and volute is significantly optimized.

Under $1.2Q_{des}$, the P_{L3} at the volute inlet surface for both models remains small. Therefore, the P_{L3} difference between the two models is small in sections 1-8. However, the P_{L3} of model B volute is significantly increased in sections 9, 10. As seen in Fig. 17, this is due to the strong rotor-stator interaction at volute tongue which severely disturbs the flow pattern in the outlet pipe. Thus, the P_{L3} in the model B volute is increased again under over-load conditions in Fig. 16(b). In conclusion, the improved flow pattern in the model B diffuser provides better volute inlet conditions and leads to the turbulence loss reduction in the volute. Under over-load conditions, the strong rotor-stator interaction at model B volute tongue lead to a surge of turbulent loss in the volute outlet pipe.

The pressure variation in the volute was studied and Fig. 19 shows the C_{sp} distribution in the volute under three conditions. The horizontal coordinates indicate volute section and the vertical coordinates indicate surface average of C_{sp}. The C_{sp} in the volute gradually decreases as the increased flow rate. The C_{sp} of both models increases with increased volute section area under $0.8Q_{des}$. Model B has a slightly lower C_{sp} in sections 1-7 than model A. This is due to the increased flow rate as seen in Fig. 17. The C_{sp} of model B is significantly increased and greater than model A in sections 8-10. In addition, the model B has an increased slope of C_{sp} curve. It can be concluded that the pressure expansion capacity of the model B volute is increased under part-load conditions.

The C_{sp} distribution of model A shows a smooth upward trend under $1.0Q_{des}$. The C_{sp} at all sections of the model B volute is significantly larger than model A volute, and the slope of C_{sp} curve is less variable. Model B has a more rapid rise of C_{sp} in the volute outlet pipe and the pressure expansion capacity is significantly enhanced. Under $1.2Q_{des}$, the slopes of C_{sp} curves are small for both models, i.e. the pressure expansion capacity in the volute is poor. As seen in the red frame, the C_{sp} curves for both models fluctuate considerably in sections 8-10. Meanwhile, the C_{sp} at the model B volute outlet pipe is lower than model A. This corresponds to the confused flow pattern and high P_{L3} at the volute outlet pipe in Figs. 17, 18.

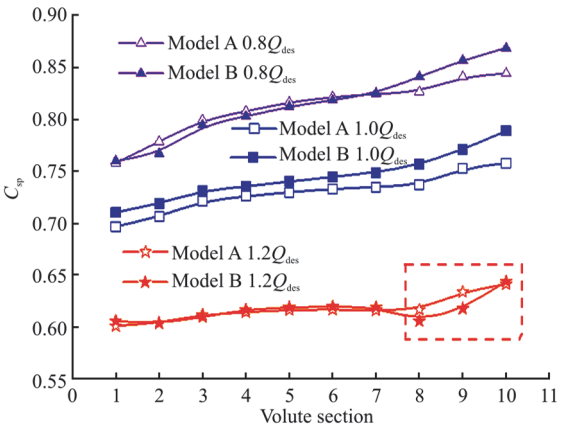

Fig. 19 (Color online) Pressure distribution in the volute

In conclusion, with the matching optimization between the diffuser and volute, the pressure expansion capacity of model B volute is enhanced under design and part-load conditions. Especially the improvement is more obvious in sections 8-10.

4. Conclusions

This study provides a detailed analysis of energy loss and flow patterns in HVCP. The emphasis is on the detailed analysis of reasons for pump performance improvement from the perspective of hydraulic components matching. The main conclusions obtained are as follows:

(1) The η, H of model B is significantly increased under design and part-load conditions. Model B solves the problem that the maximum η of model A biased towards over-load conditions. The hydraulic loss in HVCP mainly come from the diffuser and volute. And P_{L3} is the main source of energy loss in the diffuser and volute, followed by P_{LW}. The significant P_{L3} reduction in diffuser and volute is the main reason for the pump performance improvement, especially P_{L3} is greatly reduced under part-load conditions.

(2) The matching optimization between the impeller outlet flow angle and diffuser inlet vane angle results in better flow pattern in the circum-

ferential and axial directions of the diffuser and then causes significant P_{L3} reduction. The increased V_m at model B diffuser inlet regions lead to a better overflow capacity at diffuser middle and outlet regions. The matching optimization between impeller and diffuser results in most P_{L3} reduction in the model B diffuser under part-load conditions. Meanwhile, the pressure expansion capacity at vaneless and inlet regions of model B diffuser is significantly enhanced.

(3) V_t in the model B volute increases and the streamlines are more uniformly distributed under design and part-load conditions. The energy loss reduction in the volute mainly results from the improved flow pattern in the diffuser channel which provides better volute inlet conditions. The P_{L3} in the model B volute is greatest reduced in small sections 1-4 and the expansion capacity is most significantly enhanced in sections 8-10 under design and part-load conditions.

Acknowledgements

This work was supported by the Jiangsu Provincial Science Fund for Distinguished Young Scholars (Grant No. BK20211547), the Technological Innovation Team Project in Colleges and Universities of Jiangsu Province (Grant No. SKJ (2021)-1) the Open Research Subject of Key Laboratory of Fluid Machinery and Engineering (Xihua University) of Sichuan Province (Grant No. LTDL-2022007) and the Graduate Research and Innovation Projects of Jiangsu Province (Grant No. KYCX23_3701).

Compliance with ethical standards

Conflict of interest: The authors declare that they have no conflict of interest. De-sheng Zhang is an editorial board member for the Journal of Hydrodynamics and was not involved in the editorial review, or the decision to publish this article. All authors declare that there are no other competing interests.

Ethical approval: This article does not contain any studies with human participants or animals performed by any of the authors.

Informed consent: Informed consent was obtained from all individual participants included in the study.

References

[1] Zhang W., Chen Z., Zhu B. et al. Pressure fluctuation and flow instability in S-shaped region of a reversible pump-turbine [J]. *Renewable Energy*, 2020, 154: 826-840.

[2] Li D., Zhu Y., Lin S. et al. Cavitation effects on pressure fluctuation in pump-turbine hump region [J]. *Journal of Energy Storage*, 2022, 47: 103936.

[3] Zhang D. S., Yang G., Zhao X. T. et al. Optimization design of vane diffuser and volute in vertical centrifugal pump based on back propagation neural network [J]. *Transactions of the Chinese Society for Agricultural Machinery*, 2022, 53(4): 130-139(in Chinese).

[4] Ma Z., Zhu B. Pressure fluctuations in vaneless space of pump-turbines with large blade lean runners in the S-shaped region [J]. *Renewable Energy*, 2020, 153(6): 1283-1295.

[5] Zeng Y. S., Zhang S. J., Tao R. et al. Experimental study on the influence of matching relationship between impeller and guide vane on the hydraulic characteristic of a vertical centrifugal pump [J]. *Journal of Hydraulic Engineering*, 2022, 53(2): 212-21(in Chinese).

[6] Savar M., Kozmar H., Sutlovic I. Improving centrifugal pump efficiency by impeller trimming [J]. *Desalination*, 2009, 249(2): 654-659.

[7] Wu C., Zhang W., Wu P. et al. Effects of blade pressure side modification on unsteady pressure pulsation and flow structures in a centrifugal pump [J]. *Journal of Fluids Engineering*, 2021, 143(11): 111208.

[8] Qin Y. L., Li D. Y., Wang H. J. et al. Investigation on the relationship between hydraulic loss and vortex evolution in pump mode of a pump-turbine [J]. *Journal of Hydrodynamics*, 2022, 34(4): 555-569.

[9] Li W., Li E., Ji L. et al. Mechanism and propagation characteristics of rotating stall in a mixed-flow pump [J]. *Renewable Energy*, 2020, 153: 74-92.

[10] Liu H., Wu X., Tan M. Numerical investigation of the inner flow in a centrifugal pump at the shut-off condition [J]. *Journal of Theoretical and Applied Mechanics*, 2013, 51(3): 649-660.

[11] Zhu X. Y., Wang F. M., Xie C. C. et al. Influence of rotor stator interaction on impeller work for centrifugal pump [J]. *Journal of Huazhong University of Science and Technology*, 2020, 48(3): 12-17(in Chinese).

[12] Si Q. R., Liao M. Q., Qiu N. et al. Research progresses on cavitation induced noise of centrifugal pump [J]. *Journal of Ship Mechanics*, 2022, 26(5): 761-773.

[13] Bachert R., Stoffel B., Dular M. Unsteady cavitation at the tongue of the volute of a centrifugal pump [J]. *Journal of Fluids Engineering*, 2010, 132(6): 061301.

[14] Feng J., Ge Z., Yang H. et al. Rotating stall characteristics in the vaned diffuser of a centrifugal pump [J]. *Ocean Engineering*, 2021, 229: 108955.

[15] Yang G., Zhang D., Yang X. et al. Study on the flow pattern and pressure fluctuation in a vertical volute centrifugal pump with vaned diffuser under near stall conditions [J]. *Journal of the Brazilian Society of Mechanical Sciences*, 2022, 44(4): 118.

[16] Li W., Liu M., Ji L. et al. Research on the matching characteristics of the impellers and guide vanes of seawater desalination pumps with high capacity and pressure [J]. *Journal of Marine Science and Engineering*, 2022, 10(1): 115.

[17] Zeng Y., Yao Z., Tao R. et al. Effects of lean mode of blade trailing edge on pressure fluctuation characteristics of a vertical centrifugal pump with vaned diffuser [J]. *Journal of Fluids Engineering*, 2021, 143(11): 111201.

[18] Lu H. Q. Matching design and research of impeller outlet and diffuser inlet in stamping and welding centrifugal pump [D]. Master Candidate, Hangzhou, China: Zhejiang

University of Technology, 2011(in Chinese).
[19] Zhu B., Tan L., Wang X. et al. Investigation on flow characteristics of pump-turbine runners with large blade lean [J]. *Journal of Fluids Engineering*, 2018, 140: 031101.
[20] Zhou L., Shi W., Lu W. et al. Numerical investigations and performance experiments of a deep-well centrifugal pump with different diffusers [J]. *Journal of Fluids Engineering*, 2012, 134: 071102.
[21] Li D., Qin Y., Wang J. et al. Optimization of blade high-pressure edge to reduce pressure fluctuations in pump-turbine hump region [J]. *Renewable Energy*, 2022, 181: 24-38.
[22] Khoeini D., Shirani E., Joghataei M. et al. Improvement of centrifugal pump performance by using different impeller diffuser angles with and without vanes [J]. *Journal of Mechanics*, 2019, 35(4): 577-589.
[23] Shi X., Lu J., Zhao L. Investigations on the influence of tandem blades on inner flow and performance characteristics of centrifugal pump [J]. *Proceedings of the Institution of Mechanical Engineers, Part E: Journal of Process Mechanical Engineering*, 2019, 234(1): 46-55.
[24] Wang W., Yuan S., Pei J. et al. Optimization of the diffuser in a centrifugal pump by combining response surface method with multi-island genetic algorithm [J]. *Proceedings of the Institution of Mechanical Engineers, Part E: Journal of Process Mechanical Engineering*, 2017, 231(2): 191-201.
[25] Menter F. R. Two-equation eddy-viscosity turbulence models for engineering applications [J]. *AIAA Journal*, 1994, 32(8): 1598-1605.
[26] Ji L., Li W., Shi W. et al. Effect of blade thickness on rotating stall of mixed-flow pump using entropy generation analysis [J]. *Energy*, 2021, 236: 121381.
[27] Zhang F., Zhu L. F., Shi X. T. et al. Influence of pump noise on the health of fish in a large pumping station [J]. *Journal of Hydrodynamics*, 2022, 34(3): 522-531.
[28] Yang G., Zhao X., Zhang D. et al. Hydraulic components' matching optimization design and entropy production analysis in a large vertical centrifugal pump [J]. *Journal of Mechanical Science and Technology*, 2021, 35(11): 5033-5048.
[29] Wilhelm S., Balarac G., Metais O. et al. Analysis of head losses in a turbine draft tube by means of 3D unsteady simulations [J]. *Flow Turbulence and Combustion*, 2016, 97(4): 1255-1280.
[30] Lu G., Zuo Z., Liu D. et al. Energy balance and local unsteady loss analysis of flows in a low specific speed model pump-turbine in the positive slope region on the pump performance curve [J]. *Energies*, 2019, 12(10): 1829.
[31] Luo X., Ye W., Huang R. et al. Numerical investigations of the energy performance and pressure fluctuations for a waterjet pump in a non-uniform inflow [J]. *Renewable Energy*, 2020, 153: 1042-1052.
[32] Li D., Wang H., Qin Y. et al. Entropy production analysis of hysteresis characteristic of a pump-turbine model [J]. *Energy Conversion and Management*, 2017, 149: 175-191.
[33] Qi B., Zhang D., Geng L. et al. Numerical and experimental investigations on inflow loss in the energy recovery turbines with back-curved and front-curved impeller based on the entropy generation theory [J]. *Energy*, 2022, 239: 122426.